



Photothermal interface with high-adhesive superhydrophobicity to construct vapor splitting module for hydrogen evolution from seawater

Wei Wang^{a,b}, Yanan Li^a, Xiao Yu^a, Li Zhang^c, Yan Wang^a, Haichuan He^a, Henan Zhao^a, Wansong Chen^a, Jianghua Li^a, Liu Deng^{a,*}, You-Nian Liu^{a,b,*}

^a Hunan Provincial Key Laboratory of Micro & Nano Materials Interfaces Science, College of Chemistry and Chemical Engineering, Central South University, Changsha, Hunan 410083, PR China

^b College of Material, Chemistry and Chemical Engineering, Hangzhou Normal University, Hangzhou, Zhejiang 311121, PR China

^c College of Chemistry and Chemical Engineering, Hunan Institute of Science and Technology, Yueyang, Hunan 414006, PR China

ARTICLE INFO

Keywords:

Seawater
Vapor splitting
Photocatalytic hydrogen evolution
Solar-driven vapor generation
High-adhesive superhydrophobicity

ABSTRACT

Direct photocatalytic hydrogen evolution from seawater is an appealing approach to migrate the crisis of carbon emissions. However, limited solar energy utilization and catalyst poisoning are two obstacles to the hydrogen evolution from seawater. Herein, a microneedle module that integrates with solar-driven vapor generation and vapor splitting to realize directly solar-driven seawater splitting has been designed. The photothermal pedestal with high-adhesive superhydrophobicity not only provides sufficient vapor generation, but also isolates harmful substances such as salt in seawater from photocatalysts. Besides, the pedestal with superhydrophobicity and photothermal effect can provide high-temperature gas–solid reaction sites for photocatalyst microneedles to thermodynamically promote the desorption of hydrogen. Thus, the integrated module exhibits a remarkable hydrogen evolution rate of 200.5 mmol g^{−1} h^{−1} in seawater. The rational design of multifunctional interfaces opens a new window for high-efficiency direct seawater splitting to hydrogen evolution.

1. Introduction

Photocatalytic H₂ evolution from seawater is considered a promising strategy to address the crisis of carbon emissions [1–3]. However, it is facing serious challenges arising from two features. Firstly, the utilization efficiency of full-spectrum solar is still limited. Most photocatalysts can only use a limited range of sunlight, typically in the ultra-violet–visible (UV–vis) range, while discarding the potentially valuable sunlight in the near-infrared (NIR) range. Secondly, impurities present in seawater, such as Cl[−], Na⁺, Mg²⁺ and Ca²⁺, can cause catalyst poisoning, leading to a decrease in activity and durability [4,5]. Generally, pre-desalination processes for seawater are used, such as reverse osmosis [6,7], ions exchange [8], and low-temperature multi-effect distillation [9]. Obviously, the energy input required and the bulk nature of pre-desalination hinder the photocatalytic system widespread application. Recently, vapor splitting system, which directly produce H₂ from seawater, is a potential alternative to water splitting, as the avoid catalyst poisoning and loss in seawater [10–13]. The vapor can be generated by methods such as high-pressure gas purging [10], vapor

pressure differences [11], hygroscopic effects [12], and photothermal effects [13]. Among them, the photothermal effect, which exploits the NIR range in sunlight for vapor generation, is predicted to be a cost-effective and energy-efficient approach [14]. Thus, a photocatalytic system integrates of vapor splitting and solar-driven vapor generation is a highly desirable and sustainable strategy for direct seawater splitting to mass-produce green H₂ [15,16]. However, most existing works neglect the wetting property modulation of the vapor generation interface (photothermal interface), which leads to the photocatalyst being exposed to the liquid and suffering from liquid–solid phase reaction and catalysts poisoning.

Endowing the photothermal interface with superhydrophobicity can effectively inhibit contact between the seawater and the photocatalysts, preventing photocatalyst poisoning by harmful impurities [17,18]. Notably, the hydrogen-bonding interaction of liquid–solid phase plays a vital role in the vapor generation rate of the photothermal interface, because it can activate water molecules to form intermediate water, which facilitates water evaporation [19,20]. However, a common superhydrophobic surface (Cassie-state) is apt to lower the liquid

* Corresponding authors at: Hunan Provincial Key Laboratory of Micro & Nano Materials Interfaces Science, College of Chemistry and Chemical Engineering, Central South University, Changsha, Hunan 410083, PR China.

E-mail addresses: dengliu@csu.edu.cn (L. Deng), liuyounian@csu.edu.cn (Y.-N. Liu).

<https://doi.org/10.1016/j.apcatb.2024.123743>

Received 1 November 2023; Received in revised form 28 December 2023; Accepted 14 January 2024

Available online 17 January 2024

0926-3373/© 2024 Elsevier B.V. All rights reserved.

infiltration to the solid and form an “air cushion”, leading to indirect contact between water and photothermal interface [21]. Meanwhile, the hydrogen-bonding interaction between the liquid and solid is significantly demised, resulting in a decreased amount of activated water and excessive energy input for water evaporation. Consequently, the photothermal interface with superhydrophobicity suffers a low vapor generation rate, due to the increase in the energy demand of water evaporation.

Herein, a microneedle module integrating with solar-driven vapor generation and vapor splitting for directly solar-driven seawater splitting to H_2 is presented. By endowing the photothermal pedestal with high-adhesive superhydrophobicity, the microneedle module exhibits stronger hydrogen-bonding interaction of liquid–solid phase, obtaining more intermediate water (35.4%) and lower equivalent water evaporation enthalpy (1644 J g^{-1}), compared with that of Cassie-state pedestal (22.6% and 2523 J g^{-1}). Thus, vapor generation rate on the pedestal increases by nearly two times ($2.04 \text{ kg m}^{-2} \text{ h}^{-1}$) over that on the Cassie-state pedestal ($1.07 \text{ kg m}^{-2} \text{ h}^{-1}$) under 1 sun irradiation, which allows the efficient vapor availability upon the photocatalyst. Meanwhile, the superhydrophobic pedestal can spatially isolate the microneedles photocatalyst from the seawater to avoid its poisoning. Furthermore, the photothermal effect of the pedestal can increase the temperature of the microneedle photocatalyst, thermodynamically facilitating the escape of H_2 . Thus, the module achieves a remarkable H_2 evolution rate in seawater ($200.5 \text{ mmol g}^{-1} \text{ h}^{-1}$), and photocatalytic activity of the microneedle module in seawater is almost equivalent to that in pure water. This photocatalytic vapor splitting system integrated highly-adhesive superhydrophobic pedestal and microneedle photocatalyst holds a new opportunity for direct H_2 evolution from seawater.

2. Experimental

2.1. Assembly of the microneedle photocatalyst module

A polydimethylsiloxane (PDMS) mold was custom-designed by Microchip Medical Technology (Jiangsu, China). The PDMS mold contains an array of 8×8 needles, with needle height, needle base diameter, and tip-to-tip distance of 5.1, 2.3, and 2.7 mm, respectively. And the pedestal has an area of $27.3 \times 27.3 \text{ mm}^2$, and a depth of 3 mm.

For the preparation of photocatalyst microneedles, polyvinyl alcohol (PVA, $M_w = 145 \text{ kDa}$, 1 g) was added into water (99 mL) and stirred at 95°C for 6 h to obtain a clear solution. Thereafter, TiO_2 nanofibers (TiO_2 NFs, 100 mg) was added into the PVA solution (1 wt%, 10 g) under vigorous stirring for 30 min. Then, 3-glycidyloxypropyltrimethoxysilane (GPTMS, 100 mg) was added dropwise into the above-mixed suspension, and stirred for 4 h. The mass ratio of TiO_2 to PVA is 1:1. Finally, the mixture was poured into the PDMS mold, and degassed for 10 min to allow the solution to flow into the microneedle cavities. The samples were then placed in a -20°C freezer for 2 h to further compact the matrix.

For the preparation of photothermal pedestal, PVA (1 g) was added into a cellulose nanofiber (CNF) suspension (1 wt%, 99 mL) and stirred at 95°C for 6 h to obtain a clear solution. Then, hydrophobic carbon black (CB, 40 mg) was added into above-mixed suspension (PVA/CNF, 10 g) under vigorous stirring for 30 min. Thereafter, vinyltrimethoxysilane (VTMS, 400 mg) was added dropwise into the above-mixed suspension, and stirred for 4 h. The mass ratio of CB to PVA and CNF is 1:5, and the mass ratio of VTMS to the mixture of PVA and CNF is 2:1. The mixture was poured into the PDMS mold, and covered the frozen needles surface. After that, the PDMS mold was placed in frozen at -20°C for 12 h. Finally, the microneedle module was obtained via freeze-drying for 36 h. For control, neat photothermal aerogel (thickness of 5 mm), photocatalyst aerogel (thickness of 5 mm) stacked upon the photothermal aerogel (thickness of 3 mm), and microneedle module with Cassie-state superhydrophobic surface were prepared, namely $\text{PCC}_{0.2}$, $\text{PT}/\text{PCC}_{0.2}$, and *s*-microneedle.

2.2. Photocatalytic performance of H_2 evolution

Photocatalytic H_2 evolution on the microneedle module were performed in a home-made reaction cell containing 300 mL of 20 v/v% methyl alcohol/seawater, and a 300 W Xe lamp (Perfectlight, Beijing, China) was used as a light source (wavelength: 280–780 nm). The solar flux was measured using a thermopile connected to a power meter (SM206, SampoMeter, China). During the photocatalytic reaction, the gases were transferred into the sample loop by a peristaltic pump and were further quantified by gas chromatography (Agilent 7890 A; N_2 carrier gas and molecular sieve-5A column), equipped with a thermal conductivity detector. The Xe lamp and the GC were regularly calibrated to ensure reproducibility. The concentration of H_2 in this reactor was tested every 60 min. And the area used in calculation H_2 evolution rate is based on the basal area of photothermal pedestal.

3. Results and discussion

3.1. Preparation of photocatalyst microneedle module

Photocatalyst microneedle module was prepared by a secondary casting procedure (Fig. 1a). Briefly, a mixture consisting of TiO_2 NFs and PVA was poured into the PDMS mold for preparing photocatalyst needles (PVA/ TiO_2). Then, another mixture consisting of PVA, CNF and CB was poured into the PDMS mold for obtaining a photothermal pedestal with 3 mm thickness ($\text{PCC}_{0.2}$). After that, the microneedle module was obtained through freeze-drying. Each microneedle module consists of 64 needles, arranged in eight rows with a center-to-center distance of 2.7 mm (Fig. S1). The microneedle is conical with a slightly convex surface and measured 5.1 mm in length and 2.3 mm in base diameter.

As shown in Fig. 1b, a vasculature was created in the photothermal pedestal by the growth of the ice crystals in the $\text{PCC}_{0.2}$ to facilitate water transport and vapor diffusion (Fig. S2) [14,22]. CB was found to be adhered to the surface of microfibers as a photothermal agent (Fig. 1c). Notably, the $\text{PCC}_{0.2}$ pedestal exhibits desired superhydrophobicity by spatially isolating the photocatalytic needles from the liquid (MeOH/seawater: 20 v/v%) for a remarkable duration of up to 15 days (Fig. 1d), owing to the existence of hydrophobic CB (20 wt%) and VTMS [23,24]. Moreover, the microneedle module can self-float upon the solution surface, due to the superhydrophobicity and ultra-low density (0.036 g cm^{-3}) of the pedestal.

The PVA/ TiO_2 needles are closely positioned on the pedestal, as displayed in Fig. S3. The SEM and EDS mapping images reveal that TiO_2 NFs are evenly dispersed across the whole needle (Fig. S4). The uniform and smooth TiO_2 NFs (diameter: 100 nm) were prepared through annealing of precursor obtained by electrospinning under air atmosphere (Fig. S5). The crystallographic structure of the photoactive TiO_2 NFs in PVA/ TiO_2 is anatase (JCPDS #21–1272; Figs. S6 and S7). Besides, the Pt nanoparticles (ca. 4–5 nm) were deposited upon TiO_2 NFs via *in-situ* photo-reduction (details in Supporting Information) before TiO_2 NFs were constructed into PVA/ TiO_2 photocatalyst needles (Fig. S8). The Pt loading on Pt/TiO_2 is 0.8 wt% (Fig. S9). Pt/TiO_2 catalyst performs a H_2 evolution rate of $22.5 \text{ mmol g}^{-1} \text{ h}^{-1}$, which far exceeds that of commercial anatase ($7.3 \text{ mmol g}^{-1} \text{ h}^{-1}$) (Fig. S10). The photocatalytic H_2 evolution rate on TiO_2 NFs may be ascribed to rich oxygen vacancies (V_{O} s) in comparison with commercial anatase (Figs. S11 and S12) [25–27]. Meanwhile, the Pt 4f XPS spectra displayed 4 $f_{7/2}$ spin-orbit characteristic of Pt^0 , Pt^{II} , and Pt^{IV} , at 70.6 and 74.0 eV (Pt^0), 71.3 and 74.9 eV (Pt^{II}) and 76.6 eV (Pt^{IV}), respectively (Fig. S12). Generally, higher chemical valence states of Pt possess high active photocatalytic H_2 evolution performance, since it inhibits the hydrogen oxidation reaction [28,29]. Furthermore, the PVA/ TiO_2 needles exhibits strong water adsorption behavior (Fig. S13 and Movie S1). Thus, the PVA/ TiO_2 needles composed of V_{O} -rich TiO_2 NFs can be an ideal interface for solid–gas reactions, due to the hydrophilicity and the photoactivity.

Supplementary material related to this article can be found online at

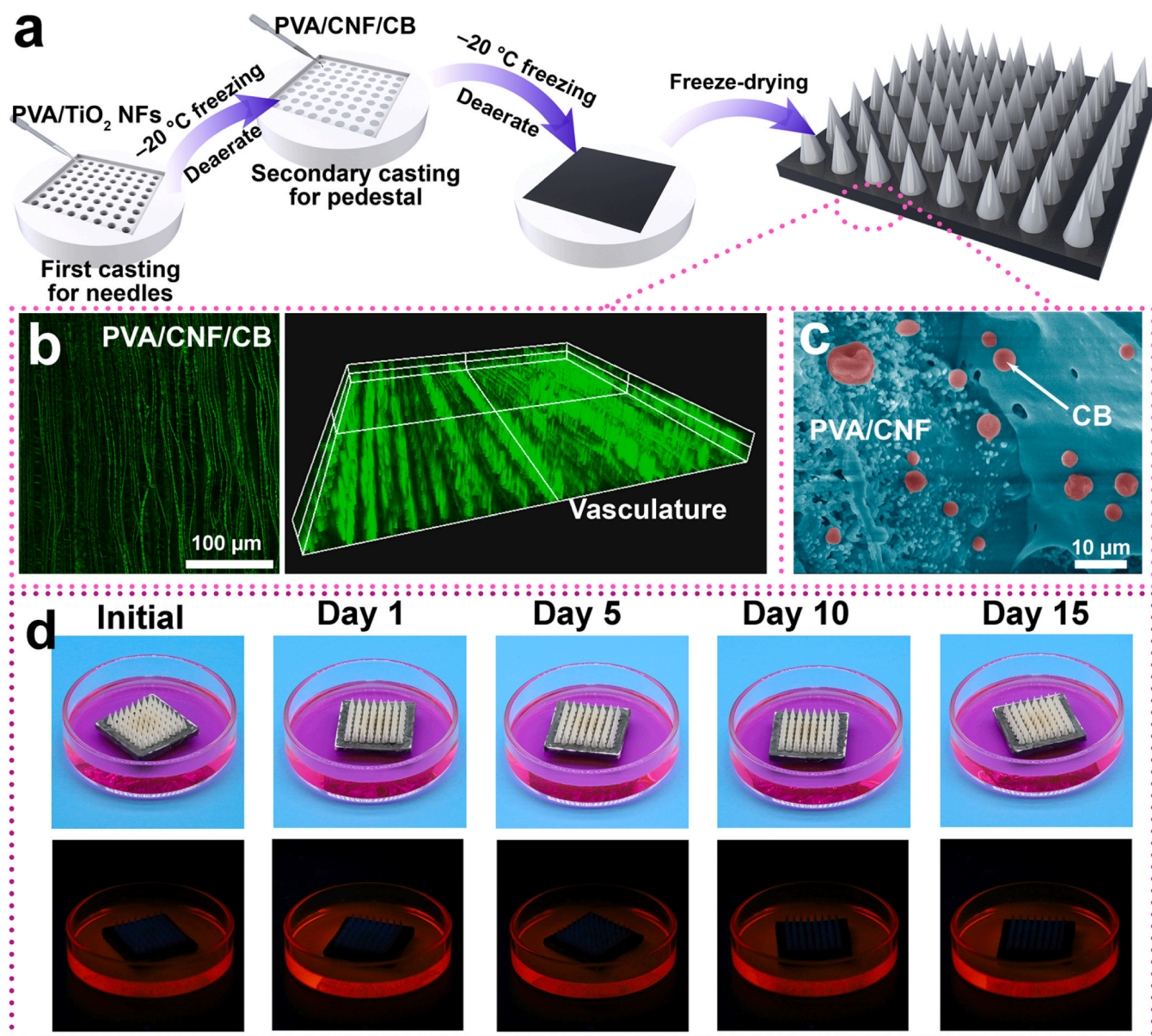


Fig. 1. Preparation of microneedle module and the superhydrophobicity of photothermal pedestal. (a) Fabrication of microneedle module using PDMS mold. (b) Confocal images of PVA/CNF/CB pedestal with 0.01% fluorescein sodium staining. (c) Pseudocolor-colored SEM images of the PVA/CNF/CB photothermal aerogel, blue: PVA/CNF skeleton, red: CB. (d) Digital images of microneedle module placed upon 20 v/v% MeOH/H₂O solution dyed by 0.1 wt% Rhodamine B.

[doi:10.1016/j.apcatb.2024.123743](https://doi.org/10.1016/j.apcatb.2024.123743).

3.2. In-situ vapor generation of the photothermal pedestal

Different superhydrophobic interfaces were prepared to investigate the influences of wetting property of the photothermal interface on vapor generation. As shown in Figs. S14–S16, s-PCC_{0.2} was prepared by spraying alkylated SiO₂ upon PCC_{0.2} surface. The liquid contact angles (CAs) of PCC_{0.2} and s-PCC_{0.2} are determined to 153.6 ± 2.4 and $151.3 \pm 3.5^\circ$, indicating the PCC_{0.2} and s-PCC_{0.2} are both superhydrophobic surface (Fig. S17). The liquid contact modes of PCC_{0.2} and s-PCC_{0.2} were further studied through the dynamic contact process and quantitative adhesive force measurement [30]. As recorded in high-speed camera images, the droplet rapidly spreads into a pancake shape within 2.53 ms on the PCC_{0.2} surface, indicating strong adhesion to the solid surface during subsequent bouncing (Fig. 2a and Movie S2). The liquid droplet quickly transforms from a pancake to a bead shape when the droplet fell on the s-PCC_{0.2} surface, and completely detaches from the solid surface

(5.06 ms). The complete bounce-off can occur multiple times, e.g., 5.06 and 20.2 ms (see Fig. 2a and Movie S3). Furthermore, an image of adsorption with a large stretch force of $124.4 \pm 0.1 \mu\text{N}$ is occurred on the PCC_{0.2} surface (see Fig. 2b and Movie S4). In contrast, the image of the negligible adsorption with extremely small stretch force of $12.5 \pm 0.7 \mu\text{N}$ is observed on the s-PCC_{0.2} pedestal (see Fig. S18 and Movie S5). These results reveal that PCC_{0.2} is of high-adhesive superhydrophobicity, while opposite for s-PCC_{0.2} (Fig. S19).

Supplementary material related to this article can be found online at [doi:10.1016/j.apcatb.2024.123743](https://doi.org/10.1016/j.apcatb.2024.123743).

To further investigate the interfacial contact of liquid–solid of PCC_{0.2} and s-PCC_{0.2}, a 3D geometry of the interface below the liquid droplet was observed via a confocal laser scanning microscope (CLSM) (Fig. S20) [31]. When the laser beam is focused at the liquid–solid interface, the intensity of the reflected laser beam is high due to the high reflection of the solid, resulting in the appearance of a peak. The liquid–gas–solid interface is the exact opposite, thus producing a trough. As depicted in Fig. 2c, the 3D image of PCC_{0.2} exhibit a uniformly distributed

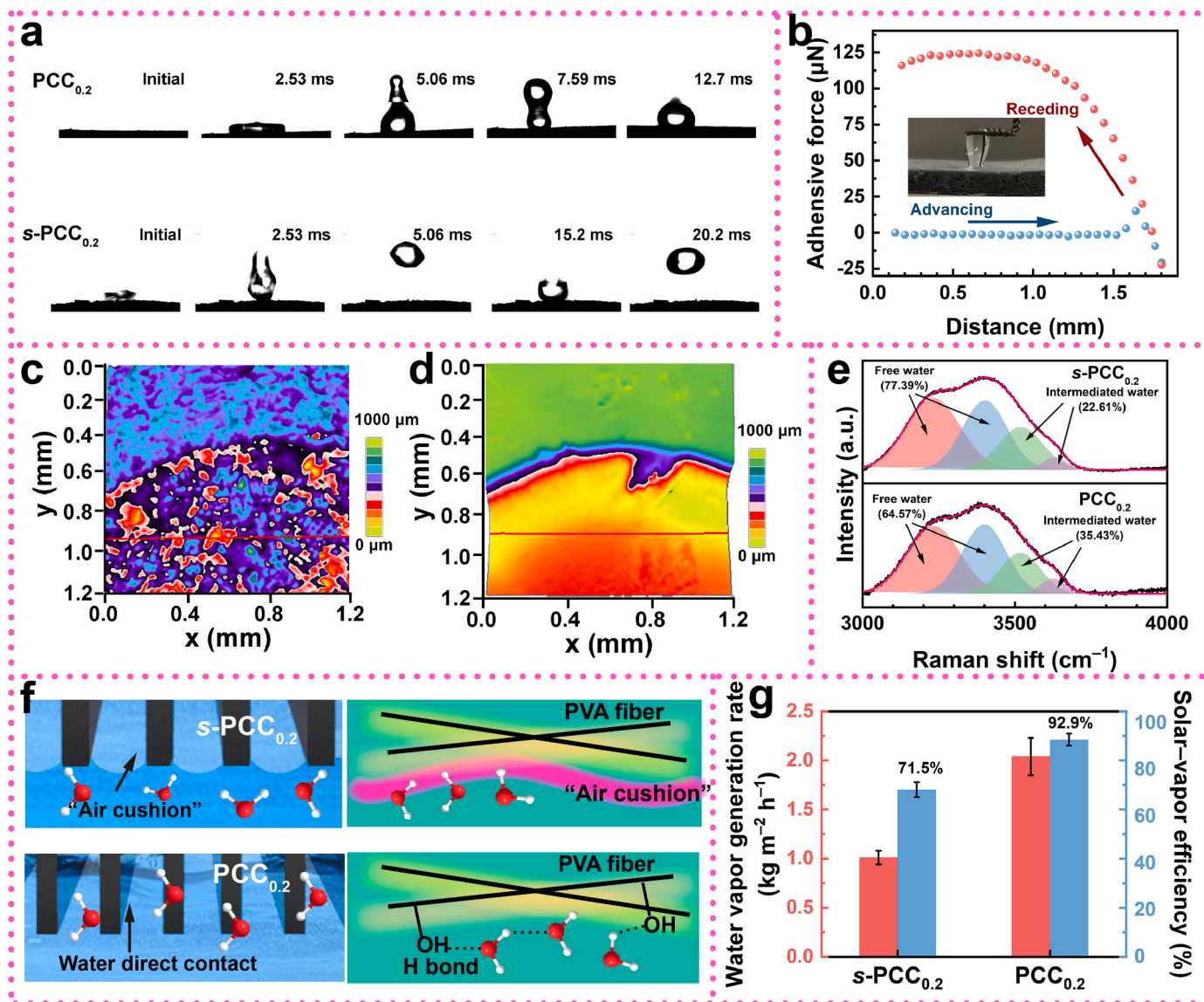


Fig. 2. Relationship between liquid contact model and water evaporation rate. (a) Time-resolved images of a 10 μL droplet falling on $\text{PCC}_{0.2}$ and $s\text{-PCC}_{0.2}$. (b) The adhesive force and digital images of receding process of the liquid droplet (10 μL) contact with $\text{PCC}_{0.2}$. (c, d) 3D images of the interfaces between the 10 μL droplet and (c) $\text{PCC}_{0.2}$ and (d) $s\text{-PCC}_{0.2}$. (e) Raman spectrum with fitting curves showing free and intermediated water on $\text{PCC}_{0.2}$ and $s\text{-PCC}_{0.2}$ exposed to 3.5% NaCl. (f) Schematic illustration of hydrogen-bonding interaction between water and solid interface on $\text{PCC}_{0.2}$ and $s\text{-PCC}_{0.2}$. (g) Vapor generation rate and efficiency of various samples in 3.5% NaCl solution at 1 sun solar irradiation for 1 h ($\theta_{\text{inc}} = 0^\circ$).

micro-/non-structure that permeates into the droplet to form the liquid–solid interface (low-reflection, peak region), while only a small portion of the surface is covered by trapped air (high-reflection, trough region). In contrast, for $s\text{-PCC}_{0.2}$, a cliff-like sudden depression appears in the area covered by droplets, indicating homogeneous air layer formation (Fig. 2d). Thus, when $\text{PCC}_{0.2}$ contact with the liquid, water is prone to infiltrate into the vasculature through capillarity. Conversely, an “air cushion” is covered upon $s\text{-PCC}_{0.2}$ surface, preventing the liquid from contacting with the surface [31–33].

Raman spectra in the region of O–H stretching of water on $\text{PCC}_{0.2}$ or $s\text{-PCC}_{0.2}$ were measured. As shown in Fig. 2e, the Raman spectra of $\text{PCC}_{0.2}$ or $s\text{-PCC}_{0.2}$ can be fitted with free water (3230 and 3400 cm^{-1}) and intermediate water (3520 and 3630 cm^{-1}) through the Gaussian function. The ratio of intermediate water to overall water on $s\text{-PCC}_{0.2}$ is only 22.6%, consistent with that of reported bulk water [34,35], while the ratio of intermediate water to overall water on $\text{PCC}_{0.2}$ increases to 35.4%. It indicates that the presence of the “air cushion”, hinders the hydrogen-bonding interaction between $s\text{-PCC}_{0.2}$ and the liquid

compared with $\text{PCC}_{0.2}$ (Fig. 2f). The equivalent evaporation enthalpy of simulated seawater on $\text{PCC}_{0.2}$ and $s\text{-PCC}_{0.2}$ is 1644 and 2523 J g^{-1} , respectively. Noted that, the equivalent evaporation enthalpy of pure water is 2460 J g^{-1} [14]. It indicates that water can be activated on the $\text{PCC}_{0.2}$ surface, resulting in less energy for evaporation (Figs. S21 and S22) [14,21]. The simulated seawater evaporation rate on $\text{PCC}_{0.2}$ is up-to $2.04 \text{ kg m}^{-2} \text{h}^{-1}$ under 1 sun irradiation, much higher than that on $s\text{-PCC}_{0.2}$ ($1.07 \text{ kg m}^{-2} \text{h}^{-1}$). Thus, the solar-to-vapor efficiency on $\text{PCC}_{0.2}$ is up to 92.9%, compared with that on $s\text{-PCC}_{0.2}$ at 71.5% (Fig. 2g).

The solar utilization efficiency and photothermal effect were further investigated. As shown in Fig. 3a, the photothermal module shows a complementary and staggered light absorption compared to the photocatalytic needles through the UV–vis–NIR spectra. Further, the surface temperature of $\text{PCC}_{0.2}$, microneedle module and PT/ $\text{PCC}_{0.2}$ is determined to be 154, 127 and 87°C via IR images after 5-min irradiation, respectively (Fig. 3b and 3c). Compared with $\text{PCC}_{0.2}$, the solar-to-heat efficacy of microneedle module maintains 82%, while that of PT/ $\text{PCC}_{0.2}$ remains only 57%, which may be originated from the NIR light

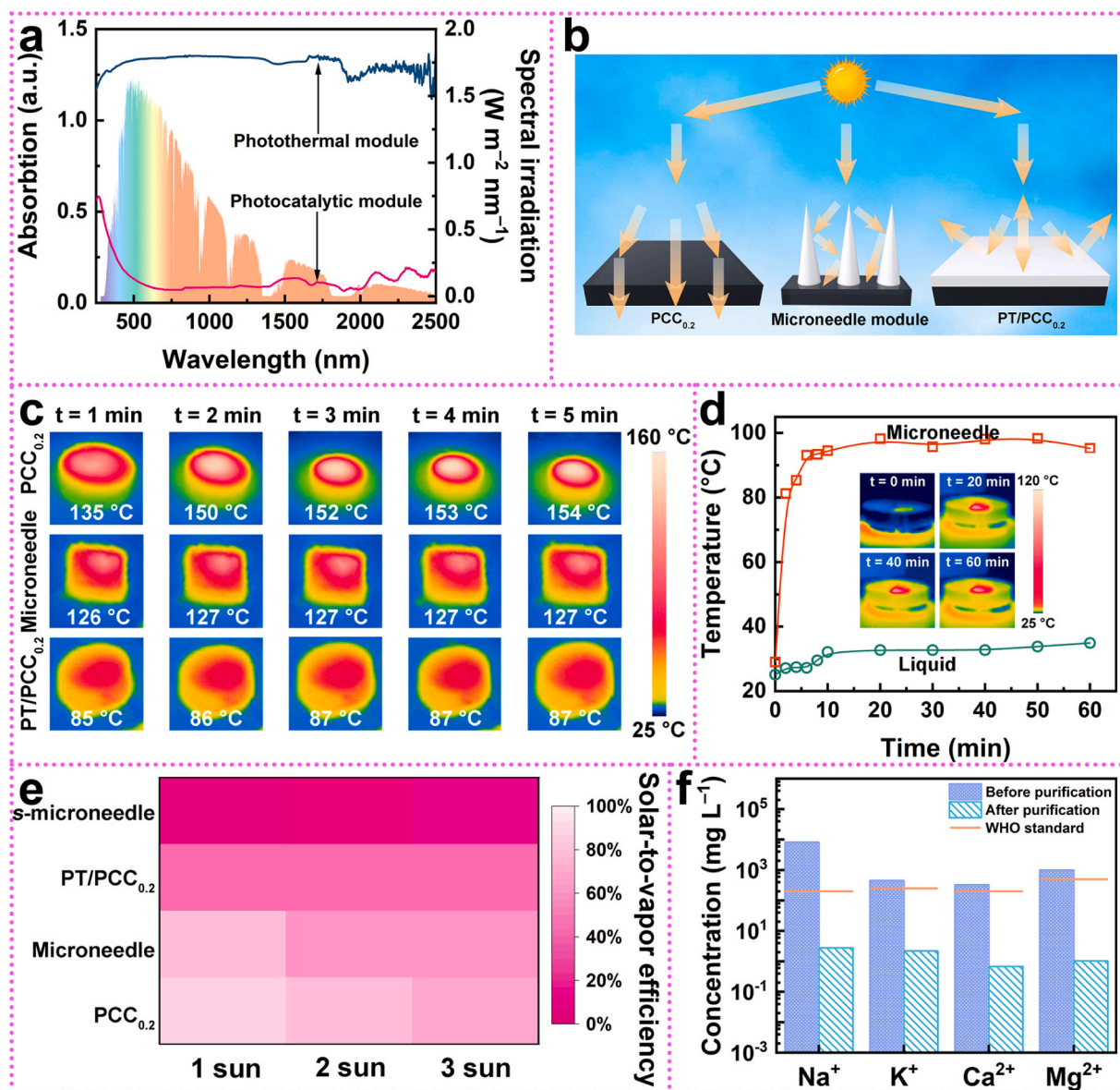


Fig. 3. Interfacial solar-heating and vapor generation. (a) UV-vis-NIR spectra of photothermal and photocatalyst aerogel, 250–2500 nm (vertical incident $\theta_{\text{inc}} = 0^\circ$), and the normalized spectral solar irradiance density of air mass 1.5 global (AM 1.5 G) tilt solar spectrum. (b) Schematic illustration of neat photothermal aerogel ($\text{PCC}_{0.2}$), microneedle module, and photocatalytic aerogel stacked on top of photothermal aerogel (PT/ $\text{PCC}_{0.2}$) in light absorption. (c) IR images of the $\text{PCC}_{0.2}$, microneedle module and PT/ $\text{PCC}_{0.2}$ at 3 sun solar simulator irradiation ($\theta_{\text{inc}} = 0^\circ$). (d) Temperature evolutions on the microneedle module surface and bulk 20 v/v% MeOH/seawater solution, the insets show the IR images of the temperature distributions at different time points. (e) Solar-to-vapor efficiency of various samples in 20 v/v% MeOH/ H_2O solution at 1, 2, or 3 sun solar simulator irradiation. (f) Measured concentrations of four primary ions in an actual seawater sample before and after desalination.

reflectivity of PT of up to 80% (Fig. S23). These results verify that the array photocatalysts aerogel can maximum the solar utilization and obtain sufficient photothermal effect. Besides, the microneedle module can be rapidly heated to 71, 100 and 127 $^\circ\text{C}$ within 1 min under the irradiation of 1, 2 and 3 sun respectively, suggesting that the microneedle spatial distribution can fulfill the requirement for sufficient solar energy input on the photothermal pedestal (Fig. S24). Moreover, the effect of the content of CB on the solar-to-heat of the pedestal was measured. As illustrated in Fig. S25, when CB accounts for 20 wt% of the total polymer mass ($\text{PCC}_{0.2}$), $\text{PCC}_{0.2}$ shows the best solar-to-heat, and therefore $\text{PCC}_{0.2}$ was used in the experiments.

Vapor feedstock generation rate and the composition of the produced vapor feedstock were evaluated over 1 h and calibrating with the dark evaporation rate. When the microneedle module placed upon the seawater under simulated sunlight of 3 sun, the surface temperature on

microneedle module increased from 29 to 95 $^\circ\text{C}$ within 10 min, and gradually increased to 98 $^\circ\text{C}$ within 60 min (Fig. 3d). In contrast, the temperature of the bulk liquid increased slightly from 25 to 35 $^\circ\text{C}$ within 60 min, which can be attributed to the low thermal conductivity ($0.035 \text{ W m}^{-1} \text{K}^{-1}$) of $\text{PCC}_{0.2}$ [14]. The evaporation rate of seawater on microneedle module reaches 8.9 (1 sun), 14.4 (2 sun), and 20.9 (3 sun) $\text{kg m}^{-2} \text{h}^{-1}$ (Fig. S26). In the case of 3 sun irradiation, the vapor feedstock generation rate on microneedle module is $20.9 \text{ kg m}^{-2} \text{h}^{-1}$, 2.7 times higher than that on PT/ $\text{PCC}_{0.2}$ ($7.7 \text{ kg m}^{-2} \text{h}^{-1}$) and 17 times higher than that on s-microneedle module (equipped with Cassie state s- $\text{PCC}_{0.2}$, $1.2 \text{ kg m}^{-2} \text{h}^{-1}$), which is close to that on neat $\text{PCC}_{0.2}$ ($21.6 \text{ kg m}^{-2} \text{h}^{-1}$).

Furthermore, another important parameter to access the *in-situ* water purification and vapor feed replenishment capabilities of microneedle, namely solar-to-vapor efficiency (η) were tested. η is defined by the following formula, [14].

$$\eta = m \Delta H_e / U_{in} \times 100\% \quad (1)$$

where m is the mass flux, ΔH_e is the equivalent vaporization enthalpy of MeOH/seawater in various samples (Fig. S27), and U_{in} is the solar irradiation power (1, 2, or 3 kW m⁻²). As illustrated in Fig. 3e, the η of microneedle and PCC_{0.2} is considerably close at different irradiation intensities, e.g., 85% for PCC_{0.2} and 77% for microneedle at 1 sun irradiation (1 kW m⁻²). However, the η of PT/PCC_{0.2} are drastically reduced to 45% for PT/PCC_{0.2} under 1 sun irradiation. It indicates that the spatial distribution of microneedles does not reduce the solar-to-vapor conversion of the photothermal pedestal. Notably, *s*-microneedle has the lowest solar-to-vapor efficiency at all irradiation intensities, which further shows the importance of the modulation of the wetting properties of the pedestal.

Besides, the concentration of several typical ions in the vapor were determined and compared with untreated seawater via ICP-AES. As shown in Fig. 3f, the microneedle module can purify high salinity

seawater into salt-free vapor under the irradiation of sunlight, which meets requirement of photocatalytic H₂ evolution. It is worth noting that the vapor produced by microneedle is a mixture of MeOH and water (the ratio of MeOH to H₂O is 17 v/v%) through the GC measurements (Figs. S28 and S29). As a sacrificial agent, MeOH can suppress oxygen production and avoid the explosion caused by the mixing of H₂/O₂ in the photocatalysis [28]. Besides, due to the arbitrary miscibility of MeOH and water, the concentration of MeOH could be greatly reduced by using a gas washing device containing water (from 17 to 0.9 v/v% after twice washing) (Fig. S29).

3.3. Photocatalytic performance of the microneedle module for direct seawater splitting

The photocatalytic H₂ evolution on microneedle in real seawater (collected from the Yellow Sea, China) was evaluated (Fig. 4a and S30). The reaction line includes a nitrogen flow rate controller, Xe lamp (light

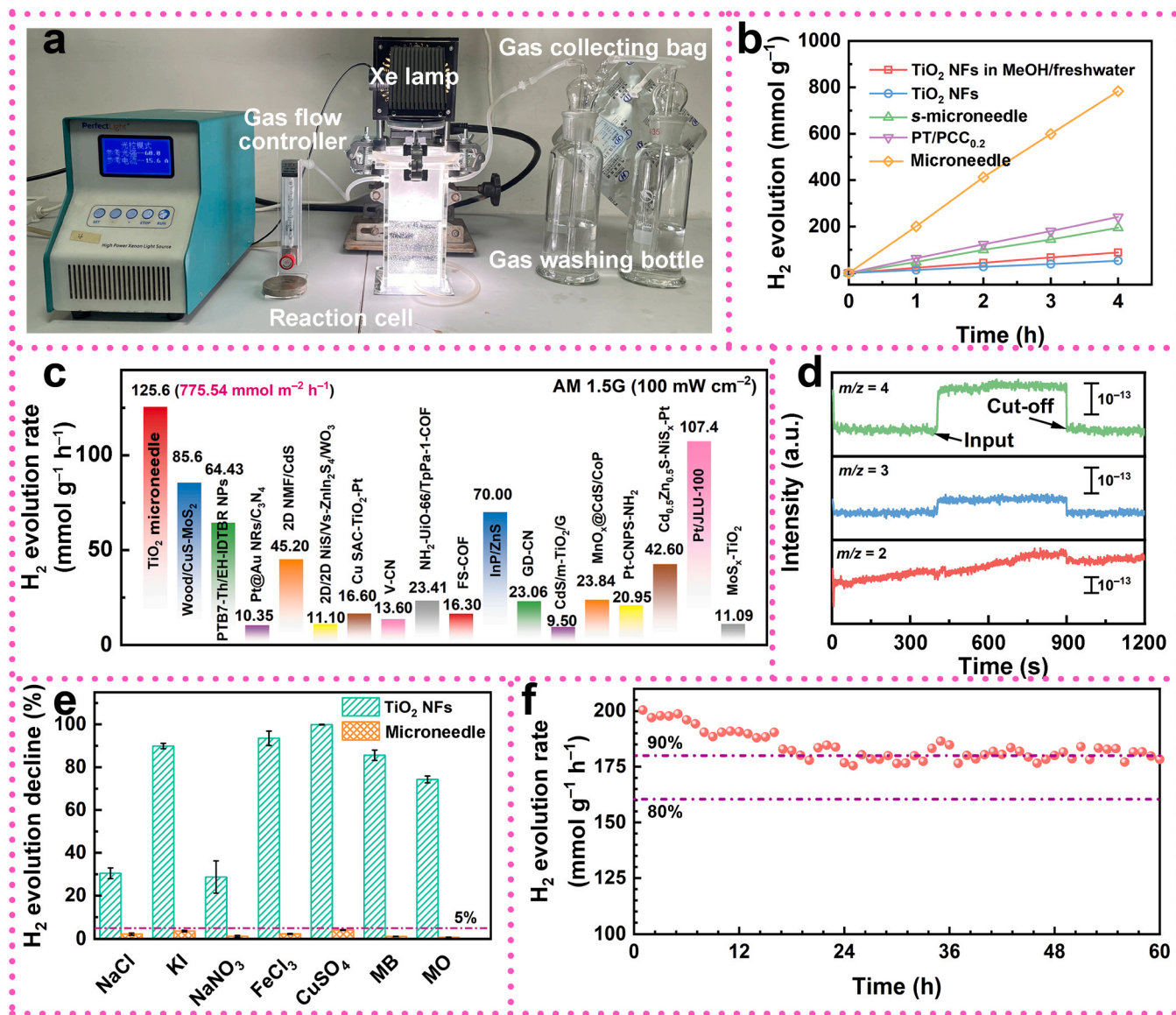


Fig. 4. Photocatalytic water vapor splitting on microneedle module. (a) Photographic images of a photocatalytic water vapor splitting system under ambient condition. (b) The photocatalytic H₂ evolution rate of samples under irradiation of 300 W Xe lamp, reaction liquid: 20 v/v% MeOH in seawater, flow rate of carrier gas (N₂): 10 mL min⁻¹, and co-catalyst: 1 wt% Pt. (c) Comparison of the H₂ evolution rate on different particle photocatalysts or photocatalysts module. The light source is a solar simulator at AM 1.5 G illumination (100 mW cm⁻²). (d) DEMS signals at $m/z = 2, 3$ and 4 over the microneedle module in 20 v/v% MeOH in D₂O solution. (e) Decline rate of photocatalytic H₂ evolution about microneedle module or TiO₂ NF powder in various sewage. (f) Recycling performance of the microneedle module.

source, 300 W), reaction cell (storage of 20 v/v% MeOH/seawater), gas washing device (for removing MeOH), and gas collection device. As displayed in Fig. 4b, the photocatalytic H_2 evolution rates on micro-needle, PT/PCC_{0.2}, and s-microneedle in real seawater are 200.5, 63.1 and 47.3 mmol g⁻¹ h⁻¹, respectively. Most importantly, the photocatalytic H_2 evolution on the microneedle module at AM 1.5 G (100 mW cm⁻²) exhibits a remarked rate of 125.6 mmol g⁻¹ h⁻¹ (775.5 mmol m⁻² h⁻¹), which superior the latest reported literature, including typical particulate photocatalysts and photocatalyst modules (Fig. 4c) [13,36–51]. Furthermore, to confirm that the produced H_2 is from catalytic water vapor splitting rather than MeOH, the *in-situ* differential electrochemical mass spectroscopy (DEMS) was carried out by using MeOH and deuterated water (D₂O) as the reactants. As shown in Fig. 4d, the signal at $m/z = 2$ (H_2) is hardly observed, whereas the signals at $m/z = 3$ (HD) or $m/z = 4$ (D₂) are sensitively responsive to the gas input and cut-off. The appearance of the signal at $m/z = 3$ (HD) may come from the hydrogen proton exchange between MeOH and water in the liquid environment [52]. These results indicate that the gaseous product is H_2 and the H atoms originate from the water vapor rather than MeOH.

In addition, the photocatalytic H_2 evolution rates on TiO₂ NFs in the

MeOH/freshwater and real seawater are 22.5 and 16.8 mmol g⁻¹ h⁻¹, and the decline rate reaches 30.4%. In contrast, the decline rate on microneedle is only 2.2% when the substrate was switched from MeOH/freshwater to MeOH/seawater. Especially, the decline rates of photocatalytic H_2 production on the microneedle module are less than 5% in various types of sewage, including NaCl saline (3.5 wt%), KI (100 mg mL⁻¹), NaNO₃ (100 mg mL⁻¹), FeCl₃ (100 mg mL⁻¹), CuSO₄ (10 mg mL⁻¹), methylene blue (MB, 200 µg mL⁻¹) and methyl orange (MO, 200 µg mL⁻¹) (Fig. 4e). By comparison, the photocatalytic H_2 evolution rate on TiO₂ NFs decreased by 99.9% in liquid reaction system (10 mg mL⁻¹ CuSO₄). Besides, after up to 60 h of operation, the micro-needle still maintains a photocatalytic H_2 evolution rate of nearly 90% (Fig. 4f). These results indicate that the microneedle can efficiently generate H_2 with long durability even in the various sewage.

The excellent photocatalytic activity and durability can be originated from the following two reasons. Firstly, the superhydrophobicity of photothermal pedestal provides the improved molecular dynamic behavior of gas-involved photocatalytic process at the gas–solid interface, in comparison with the conventional liquid–solid interface. As shown in Fig. 5a, two types of structure were constructed in the molecular dynamics simulations for analyzing possible desorption

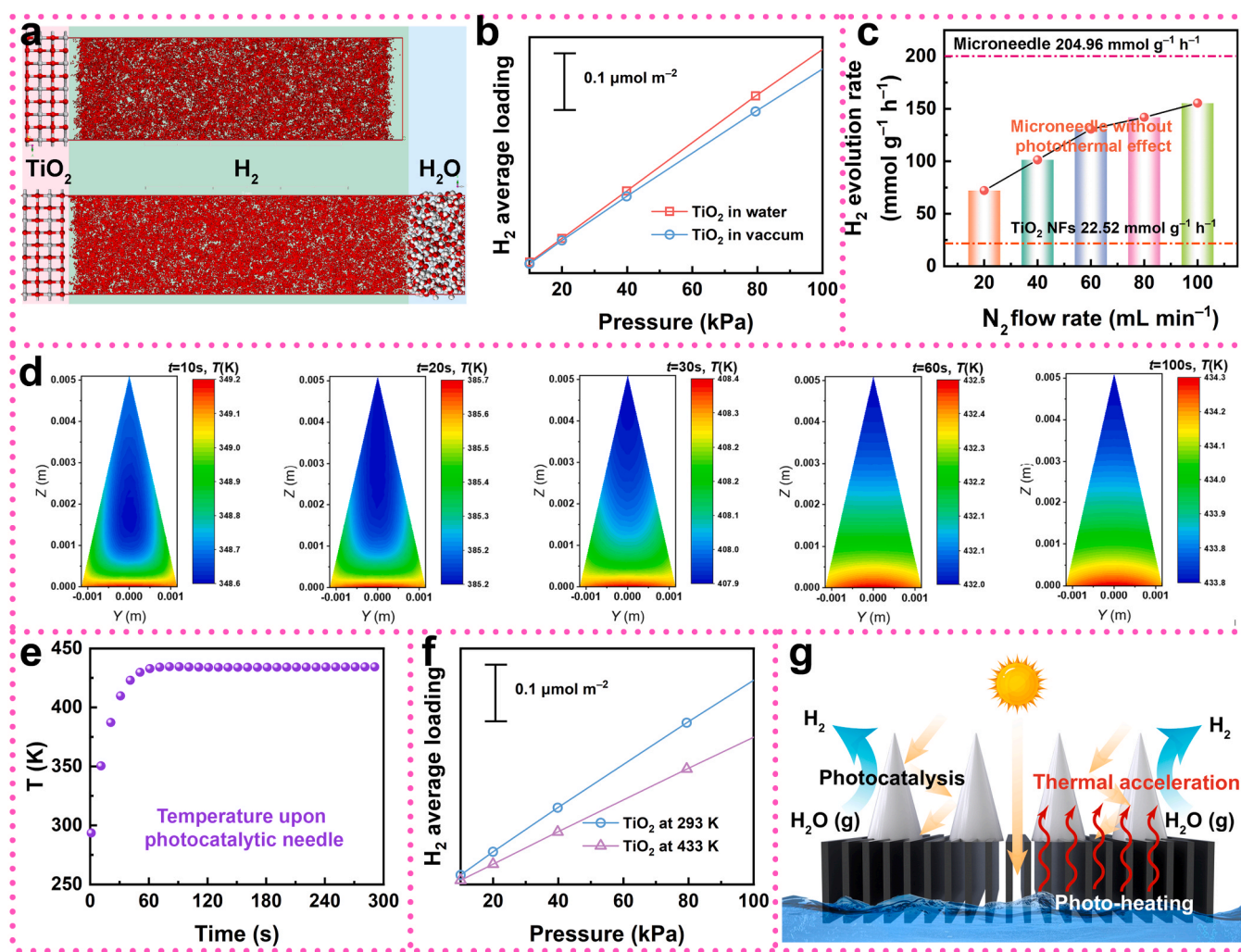


Fig. 5. Factors on the improvement of photocatalytic vapor splitting for H_2 evolution. (a) Two types of structures in the simulations of H_2 gas desorption from TiO₂ surface, i.e., TiO₂ crystal with a vacuum (top, type A) and one layer of TiO₂ and one layer of H₂O with vacuum gap (bottom, type B). (b) Adsorption isotherms for types A and B with vacuum gap size 5 nm. (c) Photocatalytic H_2 evolution rate of PVA/TiO₂-based aerogel under different gas flow rate (H₂O feed rate), irradiated by 300 W Xe lamp. (d) Temperature multi-slices of the fem simulation results. The figures were drawn by COMSOL. (e) Averaged temperature of photocatalytic needle surface rises over time. (f) Isotherms of H_2 average loading of types A at temperature 293 K and 433 K with vacuum gap size 5 nm. (g) Schematic of the improvement mechanism of photocatalytic hydrogen evolution upon the microneedle.

behavior: TiO₂ crystal with a vacuum on the surface (type A), and one layer of TiO₂ and one layer of H₂O with vacuum gaps (type B). The vacuum gap size of all them is 5 nm and the surface directions are (101) as shown in the isotherms of two cases at 293 K (Fig. 5b), indicating the improved transportation of generated hydrogen gas molecules at the gas–solid catalyst interface.

Notably, the photocatalytic H₂ evolution rate on the microneedle module without photothermal effect is much lower than that on the microneedle (205 mmol g^{−1} h^{−1}), even with an exaggerated flow rate of 100 mL min^{−1} and air humidity of 100 RH% (155.4 mmol g^{−1} h^{−1}) (Fig. 5c). As shown in Fig. 5d and 5e, the surface temperature on needles can rise to 433 K within 1 min and maintained dynamically still thereafter through the finite element method simulation. Meanwhile, the H₂ average loading at 433 K is lower than that at 293 K, indicating that higher temperature results in improved desorption behavior of H₂ gas (Fig. 5f). The second important factor of photocatalytic H₂ evolution improvement is that the photothermal effect of pedestal can increase the temperature of the photocatalyst microneedles, which can accelerate the desorption of hydrogen (Fig. 5g).

4. Conclusion

In conclusion, a microneedle module for H₂ evolution directly from seawater, which integrating with solar-driven vapor generation and photocatalytic vapor splitting has been designed. The solar-driven vapor generation used NIR range of sunlight, and the photocatalytic used UV–vis range of sunlight, realizing full-spectrum utilization of solar. By regulating wetting property, the photothermal pedestal of this microneedle module not only isolates the impurities in seawater from the photocatalysts, but also provides sufficient vapor generation. Besides, this pedestal with superhydrophobicity and photothermal effect owns a high-temperature reaction interface of gas–solid for photocatalytic needles, thermodynamically facilitate the escape of the hydrogen, thus promoting H₂ evolution rate. Therefore, the microneedle module exhibits a remarkable hydrogen evolution rate in real seawater (200.5 mmol g^{−1} h^{−1}). This integrated photocatalytic vapor splitting system holds great potential for hydrogen evolution directly from seawater.

CRedit authorship contribution statement

Liu You-Nian: Conceptualization, Formal analysis, Funding acquisition, Methodology, Project administration, Supervision, Writing – review & editing. **Wang Wei:** Conceptualization, Data curation, Formal analysis, Writing – original draft, Investigation, Methodology. **Li Yanan:** Data curation, Formal analysis, Methodology. **Zhao Henan:** Methodology, Visualization. **Chen Wansong:** Conceptualization, Formal analysis, Visualization. **Li Jianghua:** Formal analysis, Investigation, Methodology. **Deng Liu:** Conceptualization, Formal analysis, Funding acquisition, Methodology, Supervision, Writing – review & editing. **Yu Xiao:** Data curation, Formal analysis. **Zhang Li:** Data curation, Formal analysis. **Wang Yan:** Data curation, Methodology. **He Haichuan:** Formal analysis, Methodology.

Declaration of Competing Interest

The authors declare that they have no known competing financial interests or personal relationships that could have appeared to influence the work reported in this paper.

Data Availability

Data will be made available on request.

Acknowledgment

This work is supported by the National Natural Science Foundation of China (Nos. 22238013, and 22178393), the Hunan Provincial Science and Technology Plan Project, China (Nos. 2019TP1001, 2020JJ3044, and 2023JJ40706). The authors extend their gratitude to Prof. Jie Zhao and Prof. Yong Fan from Jilin University for providing valuable assistance with the testing and suggestions.

Conflict of interest

The authors declare that they have no known competing financial interests or personal relationships that could have appeared to influence the work reported in this paper, and state that the manuscript is original and is not under consideration for publication elsewhere and is approved by all authors.

Appendix A. Supporting information

Supplementary data associated with this article can be found in the online version at doi:10.1016/j.apcatb.2024.123743.

References

- [1] V. Andrei, G.M. Ucoski, C. Pornrungroj, C. Uswachoke, Q. Wang, D.S. Achilleos, H. Kasap, K.P. Sokol, R.A. Jagt, H. Lu, T. Lawson, A. Wagner, S.D. Pike, D. S. Wright, R.L.Z. Hoye, J.L. MacManus-Driscoll, H.J. Joyce, R.H. Friend, E. Reisner, Floating perovskite-BiVO₄ devices for scalable solar fuel production, *Nature* 608 (2022) 518–522, <https://doi.org/10.1038/s41586-022-04978-6>.
- [2] Y. Chen, H. Xie, M. Ma, Z. Xing, Simultaneous H₂ fuel evolution and value-added organic transformation from a one-dimensional noble-metal-free photocatalyst with spatially separated catalytic sites, *Appl. Catal. B-Environ.* 342 (2024) 123433, <https://doi.org/10.1016/j.apcatb.2023.123433>.
- [3] X. Zhang, F. Wu, G. Li, L. Wang, J. Huang, A. Meng, Z. Li, Modulating electronic structure and sulfur p-band center by anchoring amorphous Ni@NiS_x on crystalline CdS for expediting photocatalytic H₂ evolution, *Appl. Catal. B-Environ.*, (2023) 123398, <https://doi.org/10.1016/j.apcatb.2023.123398>.
- [4] C. Cheng, J. Zhang, R. Zeng, F. Xing, C. Huang, Schottky barrier tuning via surface plasmon and vacancies for enhanced photocatalytic H₂ evolution in seawater, *Appl. Catal. B-Environ.* 310 (2022) 121321, <https://doi.org/10.1016/j.apcatb.2022.121321>.
- [5] Y. Yu, W. Xu, J. Fang, D. Chen, T. Pan, W. Feng, Y. Liang, Z. Fang, Soft-template assisted construction of superstructure TiO₂/SiO₂/g-C₃N₄ hybrid as efficient visible-light photocatalysts to degrade berberine in seawater via an adsorption-photocatalysis synergy and mechanism insight, *Appl. Catal. B-Environ.* 268 (2020) 118751, <https://doi.org/10.1016/j.apcatb.2020.118751>.
- [6] L. Malaeb, G.M. Ayoub, Reverse osmosis technology for water treatment: state of the art review, *Desalination* 267 (2011) 1–8, <https://doi.org/10.1016/j.desal.2010.09.001>.
- [7] M. Elimelech, W.A. Phillip, The future of seawater desalination: energy, technology, and the environment, *Science* 333 (2011) 712–717, <https://doi.org/10.1126/science.1200488>.
- [8] J. Wang, Q. Zhang, F. Chen, X. Hou, S. Tang, Y. Shi, P. Liang, Y. Denis, Q. He, L.-J. Li, Continuous desalination with a metal-free redox-mediator, *J. Mater. Chem. A* 7 (2019) 13941–13947, <https://doi.org/10.1039/C9TA02594D>.
- [9] H. Wang, X. Wang, J. Li, H. Jing, S. Xia, F. Liu, J. Zhao, Comparison of polygorskite and struvite supported polygorskite derived from phosphate recovery in wastewater for *in-situ* immobilization of Cu, Pb and Cd in contaminated soil, *J. Hazard. Mater.* 346 (2018) 273–284, <https://doi.org/10.1016/j.jhazmat.2017.12.042>.
- [10] T. Suguro, F. Kishimoto, N. Kariya, T. Fukui, M. Nakabayashi, N. Shibata, T. Takata, K. Domen, K. Takanabe, A hygroscopic nano-membrane coating achieves efficient vapor-fed photocatalytic water splitting, *Nat. Commun.* 13 (2022) 5698, <https://doi.org/10.1038/s41467-022-33439-x>.
- [11] H. Xie, Z. Zhao, T. Liu, Y. Wu, C. Lan, W. Jiang, L. Zhu, Y. Wang, D. Yang, Z. Shao, A membrane-based seawater electrolyser for hydrogen generation, *Nature* 612 (2022) 673–678, <https://doi.org/10.1038/s41586-022-05379-5>.
- [12] J. Guo, Y. Zhang, A. Zavabeti, K. Chen, Y. Guo, G. Hu, X. Fan, G.K. Li, Hydrogen production from the air, *Nat. Commun.* 13 (2022) 5046, <https://doi.org/10.1038/s41467-022-32652-y>.
- [13] S. Guo, X. Li, J. Li, B. Wei, Boosting photocatalytic hydrogen production from water by photothermally induced biphasic systems, *Nat. Commun.* 12 (2021) 1343, <https://doi.org/10.1038/s41467-021-21526-4>.
- [14] W. Wang, Y. Wang, J. Zheng, X. Yu, W. Chen, J. Li, Y.-N. Liu, A vasculatural hydrogel combined with prussian blue for solar-driven vapor generation, *J. Mater. Chem. A* 10 (2022) 12608–12615, <https://doi.org/10.1039/d2ta02348b>.
- [15] C. Xu, S. Wu, G. Xiong, X. Guo, H. Yang, J. Yan, K. Cen, Z. Bo, K. Ostrikov, Nanoconfined fusion of g-C₃N₄ within edge-rich vertically oriented graphene hierarchical networks for high-performance photocatalytic hydrogen evolution

- utilizing superhydrophilic and superaerophobic responses in seawater, *Appl. Catal. B-Environ.* 280 (2021) 119461, <https://doi.org/10.1016/j.apcatb.2020.119461>.
- [16] P. Zhou, I.A. Navid, Y. Ma, Y. Xiao, P. Wang, Z. Ye, B. Zhou, K. Sun, Z. Mi, Solar-to-hydrogen efficiency of more than 9% in photocatalytic water splitting, *Nature* 613 (2023) 66–70, <https://doi.org/10.1038/s41586-022-05399-1>.
- [17] H. Piao, J. Zhao, H. Tang, R. Zhang, S. Zhang, Q. Huang, S. Zuo, Y. Liu, C. Xiao, S. Liu, On-demand switchable superamphiphilic nanofiber membrane reinforced by PET braided tube for efficient wastewater purification and photocatalytic regeneration, *Appl. Catal. B-Environ.* 341 (2024) 123300, <https://doi.org/10.1016/j.apcatb.2023.123300>.
- [18] X. Li, J. Wang, G. Yi, S.P. Teong, S.P. Chan, Y. Zhang, From waste plastic to artificial lotus leaf: Upcycling waste polypropylene to superhydrophobic spheres with hierarchical micro/nanostructure, *Appl. Catal. B-Environ.* 342 (2024) 123378, <https://doi.org/10.1016/j.apcatb.2023.123378>.
- [19] L. Cui, P. Wang, H. Che, X. Gao, J. Chen, B. Liu, Y. Ao, Co nanoparticles modified N-doped carbon nanosheets array as a novel bifunctional photothermal membrane for simultaneous solar-driven interfacial water evaporation and persulfate mediating water purification, *Appl. Catal. B-Environ.* 330 (2023) 122556, <https://doi.org/10.1016/j.apcatb.2023.122556>.
- [20] L. Cui, C. Ma, P. Wang, H. Che, H. Xu, Y. Ao, Rationally constructing a 3D bifunctional solar evaporator for high-performance water evaporation coupled with pollutants degradation, *Appl. Catal. B-Environ.* 337 (2023) 122988, <https://doi.org/10.1016/j.apcatb.2023.122988>.
- [21] D. Lu, Z. Zhou, Z. Wang, D.T. Ho, G. Sheng, L. Chen, Y. Zhao, X. Li, L. Cao, U. Schwingenschlogl, J. Ma, Z. Lai, An ultrahigh-flux nanoporous graphene membrane for sustainable seawater desalination using low-grade heat, *Adv. Mater.* 34 (2022) e2109718, <https://doi.org/10.1002/adma.202109718>.
- [22] H. Bai, Y. Chen, B. Delattre, A.P. Tomsia, R.O. Ritchie, Bioinspired large-scale aligned porous materials assembled with dual temperature gradients, *Sci. Adv.* 1 (2015) e1500849, <https://doi.org/10.1126/sciadv.1500849>.
- [23] M. Tai, B.C. Mohan, Z. Yao, C. Wang, Superhydrophobic leached carbon Black/Poly(vinyl) alcohol aerogel for selective removal of oils and organic compounds from water, *Chemosphere* 286 (2022) 131520, <https://doi.org/10.1016/j.chemosphere.2021.131520>.
- [24] S. Zeng, D. Zhang, W. Huang, Z. Wang, S.G. Freire, X. Yu, A.T. Smith, E.Y. Huang, H. Ngoun, L. Sun, Bio-inspired sensitive and reversible mechanochromisms via strain-dependent cracks and folds, *Nat. Commun.* 7 (2016) 11802, <https://doi.org/10.1038/ncomms11802>.
- [25] X. Zhang, Q. Yao, H. Wu, Y. Zhou, M. Zhu, Z.-H. Lu, Carbon-doped mesoporous TiO₂-immobilized Ni nanoparticles: oxygen defect engineering enhances hydrogen production, *Appl. Catal. B-Environ.* 339 (2023) 123153, <https://doi.org/10.1016/j.apcatb.2023.123153>.
- [26] W. Wang, Y. Wang, X. Zhao, Y. Li, H. He, L. Lian, K. Zeng, L. Wu, L. Deng, Y.-N. Liu, Surface oxygen vacancies of TiO_{2-x} enabled water transfer photocatalytic hydrogenation of nitrobenzene to aniline without use of co-catalyst, *Chem. Eng. Sci.* 285 (2024) 119645, <https://doi.org/10.1016/j.ces.2023.119645>.
- [27] W. Wang, X. Yu, H. He, Y. Wang, Y. Li, L. Deng, Y.-N. Liu, Electrochemical reconstitution of Prussian blue analogue for coupling furfural electro-oxidation with photo-assisted hydrogen evolution reaction, *Chem. Eng. J.* 465 (2023) 142865, <https://doi.org/10.1016/j.cej.2023.142865>.
- [28] Z. Jiang, R. Qi, Z. Huang, W. Shangquan, R.J. Wong, A. Lee, Impact of methanol photomediated surface defects on photocatalytic H₂ production over Pt/TiO₂, *Energ. Environ. Mater.* 3 (2020) 202–208, <https://doi.org/10.1002/eeem.2.12068>.
- [29] D. Vasilchenko, P. Topchiyan, A. Tsygankova, T. Asanova, B. Kolesov, A. Bukhtiyarov, A. Kurenkova, E. Kozlova, Photoinduced deposition of platinum from (Bu₄N)₂[Pt(NO₃)₆] for a low Pt-loading Pt/TiO₂ hydrogen photogeneration catalyst, *ACS Appl. Mater. Interface* 12 (2020) 48631–48641, <https://doi.org/10.1021/acsami.0c14361>.
- [30] F. Zhang, R. Zhao, Y. Wang, L. Han, J. Gu, Z. Niu, Y. Yuan, N. Qu, J. Meng, D. Wang, Superwetttable surface-dependent efficiently electrocatalytic water splitting based on their excellent liquid adsorption and gas desorption, *Chem. Eng. J.* 452 (2023), <https://doi.org/10.1016/j.cej.2022.139513>.
- [31] C. Luo, H. Zheng, L. Wang, H. Fang, J. Hu, C. Fan, Y. Cao, J. Wang, Direct three-dimensional imaging of the buried interfaces between water and superhydrophobic surfaces, *Angew. Chem. Int. Ed.* 49 (2010) 9145–9148, <https://doi.org/10.1002/anie.201002470>.
- [32] C. Lee, Y. Nam, H. Lastakowski, J.I. Hur, S. Shin, A.-L. Biance, C. Pirat, C.-J. Kim, C. Ybert, Two types of Cassie-to-Wenzel wetting transitions on superhydrophobic surfaces during drop impact, *Soft Matter* 11 (2015) 4592–4599, <https://doi.org/10.1039/C5SM00825E>.
- [33] Y. Liu, L. Moevius, X. Xu, T. Qian, J.M. Yeomans, Z. Wang, Pancake bouncing on superhydrophobic surfaces, *Nat. Phys.* 10 (2014) 515–519, <https://doi.org/10.1038/nphys2980>.
- [34] F. Zhu, L. Wang, B. Demir, M. An, Z.L. Wu, J. Yin, R. Xiao, Q. Zheng, J. Qian, Accelerating solar desalination in brine through ion activated hierarchically porous polyion complex hydrogels, *Mater. Horiz.* 7 (2020) 3187–3195, <https://doi.org/10.1039/d0mh01259a>.
- [35] X.M. Han, L.V. Besteiro, C.S.L. Koh, H.K. Lee, I.Y. Phang, G.C. Phan-Quang, J.Y. Ng, H.Y.F. Sim, C.L. Lay, A. Govorov, X.Y. Ling, Intensifying heat using MOF-isolated graphene for solar-driven seawater desalination at 98% solar-to-thermal efficiency, *Adv. Funct. Mater.* 31 (2021), <https://doi.org/10.1002/adfm.202008904>, 2008904–2008015.
- [36] J. Kosco, M. Bidwell, H. Cha, T. Martin, C.T. Howells, M. Sachs, D.H. Anjum, S. Gonzalez Lopez, L. Zou, A. Wadsworth, W. Zhang, L. Zhang, J. Tellam, R. Sougrat, F. Laquai, D.M. DeLongchamp, J.R. Durrant, I. McCulloch, Enhanced photocatalytic hydrogen evolution from organic semiconductor heterojunction nanoparticles, *Nat. Mater.* 19 (2020) 559–565, <https://doi.org/10.1038/s41563-019-0591-1>.
- [37] L. Zhang, N. Ding, L. Lou, K. Iwasaki, H. Wu, Y. Luo, D. Li, K. Nakata, A. Fujishima, Q. Meng, Localized surface plasmon resonance enhanced photocatalytic hydrogen evolution via Pt@Au NRs/C₃N₄ nanotubes under visible-light irradiation, *Adv. Funct. Mater.* 29 (2019) 1806774, <https://doi.org/10.1002/adfm.201806774>.
- [38] J. Ran, J. Qu, H. Zhang, T. Wen, H. Wang, S. Chen, L. Song, X. Zhang, L. Jing, R. Zheng, S.-Z. Qiao, 2D metal organic framework nanosheet: a universal platform promoting highly efficient visible-light-induced hydrogen production, *Adv. Energy Mater.* 9 (2019) 1803402, <https://doi.org/10.1002/aenm.201803402>.
- [39] Z. Li, J. Hou, B. Zhang, S. Cao, Y. Wu, Z. Gao, X. Nie, L. Sun, Two-dimensional Janus heterostructures for superior Z-scheme photocatalytic water splitting, *Nano Energy* 59 (2019) 537–544, <https://doi.org/10.1016/j.nanoen.2019.03.004>.
- [40] B.-H. Lee, S. Park, M. Kim, A.K. Sinha, S.C. Lee, E. Jung, W.J. Chang, K.-S. Lee, J. H. Kim, S.-P. Cho, H. Kim, K.T. Nam, T. Hyeon, Reversible and cooperative photoactivation of single-atom Cu/TiO₂ photocatalysts, *Nat. Mater.* 18 (2019) 620–626, <https://doi.org/10.1038/s41563-019-0344-1>.
- [41] Y. Zhang, L. Wu, X. Zhao, Y. Zhao, H. Tan, X. Zhao, Y. Ma, Z. Zhao, S. Song, Y. Wang, Y. Li, Leaf-mosaic-inspired vine-like graphitic carbon nitride showing high light absorption and efficient photocatalytic hydrogen evolution, *Adv. Energy Mater.* 8 (2018) 1801139, <https://doi.org/10.1002/aenm.201801139>.
- [42] F. Zhang, J. Sheng, Z. Yang, X. Sun, H. Tang, M. Lu, H. Dong, F. Shen, J. Liu, Y. Lan, Rational design of MOF/COF hybrid materials for photocatalytic H₂ evolution in the presence of sacrificial electron donors, *Angew. Chem. Int. Ed.* 57 (2018) 12106–12110, <https://doi.org/10.1002/anie.201806862>.
- [43] X. Wang, L. Chen, S.Y. Chong, M.A. Little, Y. Wu, W.-H. Zhu, R. Clowes, Y. Yan, M. A. Zwiijnenburg, R.S. Sprick, A.I. Cooper, Sulfone-containing covalent organic frameworks for photocatalytic hydrogen evolution from water, *Nat. Chem.* 10 (2018) 1180–1189, <https://doi.org/10.1038/s41557-018-0141-5>.
- [44] S. Yu, X.-B. Fan, X. Wang, J. Li, Q. Zhang, A. Xia, S. Wei, L.-Z. Wu, Y. Zhou, G. R. Patzke, Efficient photocatalytic hydrogen evolution with ligand engineered all-inorganic InP and InP/ZnS colloidal quantum dots, *Nat. Commun.* 9 (2018) 4009, <https://doi.org/10.1038/s41467-018-06294-y>.
- [45] Y. Yu, W. Yan, X. Wang, P. Li, W. Gao, H. Zou, S. Wu, K. Ding, Surface engineering for extremely enhanced charge separation and photocatalytic hydrogen evolution on g-C₃N₄, *Adv. Mater.* 30 (2018) 1705060, <https://doi.org/10.1002/adma.201705060>.
- [46] Y. Lu, X. Cheng, G. Tian, H. Zhao, L. He, J. Hu, S. Wu, Y. Dong, G. Chang, S. Lenaerts, S. Siffert, G. Van Tendeloo, Z. Li, L. Xu, X. Yang, B. Su, Hierarchical CdS/m-TiO₂/G ternary photocatalyst for highly active visible light-induced hydrogen production from water splitting with high stability, *Nano Energy* 47 (2018) 8–17, <https://doi.org/10.1016/j.nanoen.2018.02.021>.
- [47] M. Xing, B. Qiu, M. Du, Q. Zhu, L. Wang, J. Zhang, Spatially separated CdS shells exposed with reduction surfaces for enhancing photocatalytic hydrogen evolution, *Adv. Funct. Mater.* 27 (2017) 1702624, <https://doi.org/10.1002/adfm.201702624>.
- [48] N. Meng, J. Ren, Y. Liu, Y. Huang, T. Petit, B. Zhang, Engineering oxygen-containing and amino groups into two-dimensional atomically-thin porous polymeric carbon nitrogen for enhanced photocatalytic hydrogen production, *Energ. Environ. Sci.* 11 (2018) 566–571, <https://doi.org/10.1039/C7EE03592F>.
- [49] M. Liu, Y. Chen, J. Su, J. Shi, X. Wang, L. Guo, Photocatalytic hydrogen production using twinned nanocrystals and an unanchored NiS₂ co-catalyst, *Nat. Energy* 1 (2016) 16151, <https://doi.org/10.1038/nenergy.2016.151>.
- [50] S. Ma, T. Deng, Z. Li, Z. Zhang, J. Jia, Q. Li, G. Wu, H. Xia, S. Yang, X. Liu, Photocatalytic hydrogen production on a sp²-carbon-linked covalent organic framework, *Angew. Chem. Int. Ed.* 61 (2022) e202208919, <https://doi.org/10.1002/anie.202208919>.
- [51] T. Daeneke, N. Dahr, P. Atkin, R.M. Clark, C.J. Harrison, R. Brkljača, N. Pillai, B. Y. Zhang, A. Zavabeti, S.J. Ippolito, K.J. Borean, J.Z. Ou, M.S. Strano, K. Kalantar-zadeh, Surface water dependent properties of sulfur-rich molybdenum sulfides: electrolyteless gas phase water splitting, *ACS Nano* 11 (2017) 6782–6794, <https://doi.org/10.1021/acsnano.7b01632>.
- [52] M. Nielsen, E. Alberico, W. Baumann, H.-J. Drexler, H. Junge, S. Gladiali, M. Beller, Low-temperature aqueous-phase methanol dehydrogenation to hydrogen and carbon dioxide, *Nature* 495 (2013) 85–89, <https://doi.org/10.1038/nature11891>.